Semicond. Sci. Technol. **11** (1996) 1–16. Printed in the UK

TOPICAL REVIEW

Tunnelling spectroscopy of low-dimensional states

J Smoliner

Institut für Festkörperelektronik 362, Technische Universität Wien, Floragasse 7, A-1040 Wien, Austria

Received 22 August 1994, in final form 2 May 1995, accepted for publication 18 September 1995

Abstract. In this review a survey of tunnelling processes between barrier-separated two-dimensional (2D) systems and systems of different dimensionality is given. Tunnelling between barrier-separated 2D systems can be studied on very different samples such as triple-barrier structures, double-barrier structures with a two-dimensional emitter, double-barrier structures under hydrostatic pressure, double heterostructures, coupled quantum wells and also coupled 2D electron–hole systems. Pure 2D–2D tunnelling processes with individual contacts on both 2D systems, however, are only reported on double heterostructures and coupled quantum wells. Using a transfer Hamiltonian formalism, it is shown that all resonances in the tunnelling current have their origin in density of states effects, transmission coefficients or the overlap integrals between the initial and final states. 2D subband energies, background impurity concentrations, the effective mass and also non-parabolicity effects can be determined quantitatively in terms of the transfer Hamiltonian formalism.

By nanofabrication, tunnelling processes between 2D systems and states of lower dimensionality (1D, 0D) can also be investigated. Here, the tunnelling processes are mainly influenced by the overlap integral between the initial and final states. The corresponding resonance positions in the tunnelling current strongly depend on the shape of the confining potential and, moreover, the current–voltage characteristics turn out to be the Fourier transform of the 1D (0D) wavefunction of the final state. A brief survey of 1D–1D and 1D–0D tunnelling experiments is also given.

1. Introduction

Tunnelling spectroscopy [1] has been used to study very different types of junctions [2] over a long period of time. In particular the investigation of quantized surface states has turned out to be a highly interesting topic, since tunnelling spectroscopy is a simple and helpful tool for determining material parameters such as the electron effective mass or LO phonon energies. Tsui [3, 4] investigated the subband energies of bound states in a surface accumulation layer at InAs–InAs–oxide interfaces. Resonant tunnelling processes into these bound states were evident as peaks in the derivative of the tunnelling current, and in addition LO assisted transitions were also resolved. In strong magnetic fields applied perpendicular to the junction, the measured spacing between the Landau levels of the electric subbands allowed a determination of the effective mass of electrons in InAs. Later, similar experiments were also carried out on PbTe–PbTe–oxide junctions [5] InGaAs–oxide–Pb [6] and Si–SiO_2 junctions [7] to determine the electron effective mass and the LO phonon energy in these materials.

High-quality GaAs–AlGaAs heterostructures grown by molecular beam epitaxy allowed more extensive studies of the influence of phonons and other physical properties through tunnelling spectroscopy. In tunnelling experiments on single-barrier heterostructures, LO phonon emission causes extra structures in the tunnelling characteristics, as soon as the difference between the emitter energy and the collector Fermi level exceeds the LO phonon energy [8]. On double-barrier structures, LO phonons are evident through small satellites of the large negative differential regions, which occur each time an emitter state matches another state inside the well [9]. Moreover, normally forbidden transitions such as transitions between Landau levels of different indices, become allowed if the momentum conservation parallel to the barriers is violated by phonons [10, 11].

In contrast to earlier experiments, where the electrons tunnel from a metal through a barrier into quantized two-dimensional surface states, molecular beam epitaxy (MBE) growth made it possible to obtain samples where the tunnelling takes place entirely in the semiconductor material. The former oxide barrier is replaced by a monocrystalline semiconductor layer, which has a higher

0268-1242/96/010001+16$19.50

bandgap than the embedding material. In the case of the GaAs–AlGaAs material system, the barrier height can be varied via the aluminium concentration in the AlGaAs, and thus MBE growth offers the possibility to fabricate samples with a wide range of different barrier heights and widths. These samples have a much higher quality than the former metal–oxide–semiconductor systems and, moreover, multibarrier structures of any kind can easily be made. MBE growth also offers the possibility of fabricating samples, containing states of reduced dimensionality. Very interesting effects occur on samples with two-dimensional (2D) emitter electrodes, 2D collectors or 2D intermediate states. In the following section, these 2D–2D tunnelling processes and typical experiments are briefly described.

2. Resonant tunnelling in 2D–2D systems

The most straightforward method of realizing tunnelling between different 2D states is an asymmetric triple-barrier [12] structure on the GaAs–AlGaAs material system. The corresponding conduction band profile is shown in figure 1(a). Here the electrons tunnel from a doped GaAs emitter region through a double quantum well into a doped GaAs collector. From the 3D GaAs region, the electrons tunnel into the 2D states of the first quantum well, then transitions between the 2D states in the first well and the 2D states of the second well occur and are followed by tunnelling of the 2D electrons in the second well into the 3D collector electrode. Resonances in the tunnelling current are always observed when the Fermi energy in the emitter is aligned with the subband energies in the wells, and another peak is expected when the subband energies in the asymmetric wells are aligned. In magnetic fields applied perpendicular to the layers of the samples, however, the situation becomes more complicated. Now, Landau levels exist in both quantum wells, and a large number of different transitions can be observed, which are due to tunnelling processes between the 3D emitter and the different Landau levels inside the wells. Moreover, inter-Landau level transitions inside the wells are also expected. As it is not quite clear for such triple-barrier structures how much of the applied voltage drops across the various barriers, the quantitative analysis of the corresponding tunnelling characteristics is rather difficult.

A more controlled way of investigating tunnelling processes between two 2D systems is to use standard double-barrier structures with large undoped spacers in front of the barriers [13]. Under bias, electrons accumulate in the undoped regions. If the sample quality if high enough, 2D subbands are established in the almost triangular potential region in front of the barrier. Electrons tunnel from the 2D subbands of an accumulation layer through the empty subbands inside the barriers into a 3D collector (see figure 1(b)). Experimentally, the 2D character of the emitter electrodes is reflected in oscillations of the resonance position in strong magnetic fields applied perpendicular to the sample. Beyond the main resonance, further peaks can be observed, which correspond to elastic and inelastic scattering enhanced tunnelling processes. Note that for double barriers with a 2D emitter, the Fermi

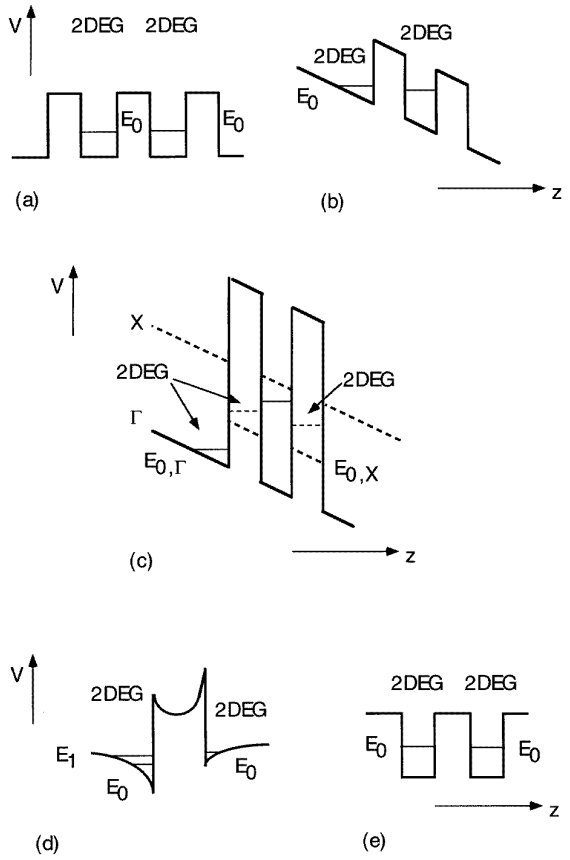

Figure 1. Conduction band profiles of typical 2D–2D tunnelling structures: (a) triple-barrier diodes, (b) double-barrier diode with 2D emitter, (c) double-barrier diode under hydrostatic pressure (Γ, X denote the Γ and X conduction band profiles), (d) double heterostructure, (e) double quantum well. E_0 denotes the lowest subband in each structure.

level is normally well below the LO phonon energy and thus phonon assisted tunnelling processes can also be studied. The above situation, where electrons tunnel from 2D and 3D emitters through a 2D state, has also stimulated some theoretical work, especially since it has turned out that the peak to valley ratio of the resonant tunnelling current is better for double-barrier structures with a 2D emitter [14]. A high peak to valley ratio is crucial for device applications and thus an understanding of the influence of phonon assisted tunnelling from 2D emitter states on the valley current yields important information for the optimization of resonant tunnelling diodes [15]. Further studies concern doping profile effects and tunnelling times of confined electrons in double-barrier heterostructures [16] and also self-consistent calculations of 3D–2D and 2D–2D resonant tunnelling processes in double-barrier diodes [17].

An elegant alternative method for investigating tunnelling processes between two-dimensional systems is to apply a sufficiently high hydrostatic pressure to an AlAs–GaAs–AlAs heterostructures [18]. This method takes advantage of the energy alignment of the Γ and X point of the Brillouin zone in the GaAs and the AlAs and the different influence of external hydrostatic pressure on

them. Figure 1(c) shows that under appropriate hydrostatic pressure the X-valley in AlAs is lower than in GaAs and electrons are transferred into the thin AlAs layers, which form two quantum wells cladded between the GaAs barriers. Thus, there are two two-dimensional electron systems in the X-valley which are separated only by a thin barrier. In the current–voltage ($I(V_b)$) curves, the tunnelling processes between the 2D states in the X-valley result in structures which occur in addition to the negative differential resistance due to the resonant tunnelling processes in the Γ-valley. These additional peaks unambiguously show that 2D–2D tunnelling is present in such a sample, but compared with the effects in the double 2D systems presented above they are rather weak.

All above systems have in common that electrons tunnel from 2D emitters through a 2D state into a 3D continuum or from a 3D emitter through two 2D states. This has the disadvantage that 3D states are always involved in the tunnelling processes, which either makes the analysis difficult or weakens the 2D effects. However, there are two different structures reported in the literature where only tunnelling processes between the 2D systems can be investigated.

The first tunnelling processes between two purely two-dimensional systems were reported by Smoliner *et al* [19, 20] on a sample having a bandstructure which is shown in figure 1(d). On such a sample, two 2D electron systems exist on both sides of the doped AlGaAs barrier. Although these 2D systems are only separated by a barrier of 200 Å, independent contacts to both channels can be achieved. Through these independent contacts, the 2D electron systems are shifted energetically with respect to each other, and thus transitions between the 2D subbands on each side of the barrier can be studied. These transitions are directly evident as peaks in the tunnelling current and its derivative. Such measurements are performed using a four-terminal conduction bridge [21], to compensate series resistances and to achieve a high resolution. This technique is crucial at strong magnetic fields, where the series resistances in the lower 2D channel becomes an oscillatory function of the magnetic field. A further advantage of this sample was found to be that, to an extremely good approximation, all of the applied voltage drops over the barrier [22] and the relative energy shift of the 2D systems are equal to $e\Delta V_b$.

It must be pointed out that for all these experiments the applied voltages are large enough to induce tunnelling processes between different subbands on each side of the barrier. For a second type of experiment, so-called equilibrium tunnelling spectroscopy [23], just very small bias voltages are used. In this way, only transitions close to the Fermi energies in both 2D channels are investigated. For these experiments, a double quantum well structure was first introduced by Eisenstein *et al* [24, 25], which is shown in figure 1(e). To establish individual contacts to the two 2D systems on this sample, a selective depletion technique using gates was applied. Ohmic contacts were alloyed through both channels simultaneously, but the individual channels are locally depleted through different gates on the top and the backside of the sample and not by an etching process. Thus it is possible to apply voltages between the channels and to perform both tunnelling experiments and magnetotransport in each individual channel. The electron concentrations in both channels can be controlled via additional frontgates and backgates on the sample. As an alternative to evaporation, the gates can also be fabricated by *in situ* ion beam lithography and molecular epitaxy regrowth, which has the advantage that patterned gate structures can be incorporated directly into the structure [26–28].

A main advantage of the double quantum well structure over the 2D double heterostructure is that it contains an undoped barrier which yields very high electron mobilities in both channels and almost no scattering during the electron transfer between the two 2D systems. This enables investigations on the influence of the second 2D channel on the normal quantum Hall [29–31] effect, device applications [32, 33], measurements and screening effects [34], and also predictions on a transmitted phonon drag between parallel two-dimensional electron gases through a Monte Carlo simulation [35].

Most recently, advanced MBE growth and contact formation have made it possible to fabricate separately contacted electron–hole double layers in GaAs–AlGaAs heterostructures [36]. Such a system becomes very interesting when the spacing between the carriers is comparable with the separating barrier width, which means that strong electron–hole interactions will be possible. For such a system, it is expected, for example, that the crystal phase boundary between the fractional quantum Hall effect and the Wigner crystal phase is changed [37]. If the layers are sufficiently close and the carriers are dilute enough, electrons and holes will form a 2D Bose gas of stable excitons that is expected to have a superfluid transition [38, 39]. Electron–hole annihilation is also possible if the barriers are thin enough, which is a promising radiation source, where the photon energy and the recombination times can be adjusted via MBE growth [40, 41].

3. The transfer Hamiltonian formalism

3.1. 2D–3D tunnelling at $B = 0$ T

As shown above, MBE growth offers the possibility for many 2D–2D tunnelling experiments on very different kinds of samples. To understand the experimental data, however, it is necessary to calculate the tunnelling current, or at least its components which contribute to the above effects. A practical method for this is the so-called transfer Hamiltonian formalism, where the initial and final states are treated as independent systems separated by the barrier. Then a time-dependent perturbation is introduced to couple the initial and final states. The transfer of electrons from one electrode to the other is caused by this perturbation and the tunnelling probability is obtained by the time-dependent evolution of the initial state. In the following, the initial states are defined to be on the left-hand side and the final states on the right-hand side of the barrier.

In what follows the transfer Hamiltonian formalism [42–44] is applied to the tunnelling processes between

barrier-separated 2D systems and also to transitions between 2D states and states of lower dimensionality. It should be mentioned, however, that the transfer Hamiltonian formalism is not restricted to this system and that it can be applied to any kind of tunnelling process.

According to Fermi's golden rule, the tunnelling probability per unit time, which is the tunnelling rate, is given as

$$P_{\mathrm{LR}} = \frac{2\pi}{\hbar}|M_{\mathrm{LR}}|^2 g_{\mathrm{R}}(E_z) f_{\mathrm{L}}(E)(1 - f_{\mathrm{R}}(E)). \qquad (1)$$

M_{LR} is the matrix element for transitions between the left- and right-hand side of the barrier, g_{R} the density of states on the final side and f the Fermi distribution function. The states on the left-hand side are defined as initial states, the states on the right-hand side as final states. The matrix element can be expressed as

$$M_{\mathrm{LR}} = -\frac{\hbar^2}{2m^*}\int\!\!\int_{z=z_0} \mathrm{d}^2 S \left(\Psi_{\mathrm{R}}^* \frac{\partial \Psi_{\mathrm{L}}}{\partial z}\bigg|_{z=z_0} - \Psi_{\mathrm{L}} \frac{\partial \Psi_{\mathrm{R}}^*}{\partial z}\bigg|_{z=z_0} \right). \qquad (2)$$

The integration over the surface elements $\mathrm{d}S$ has to be carried out in the plane of the barrier which separates the initial and final side at $z = z_0$. To calculate the tunnelling current, one has to sum over all initial and final k vectors, k_{L}. If one includes the possibility of forward and backward tunnelling and also the influence of spin, the resulting tunnelling current density is calculated as

$$j = \frac{4\pi e}{\hbar}\sum_{k_{\mathrm{L}}} |M_{\mathrm{LR}}|^2 g_{\mathrm{R}}(E_z) f_{\mathrm{L}}(E)(1 - f_{\mathrm{R}}(E))$$

$$j = \frac{4\pi e}{\hbar}\sum_{k_{x,\mathrm{L}},k_{y,\mathrm{L}}} \int \mathrm{d}E_z |M_{\mathrm{LR}}|^2 g_{\mathrm{R}}(E_z) g_{\mathrm{L}}(E_z) \times (f_{\mathrm{L}}(E) - f_{\mathrm{R}}(E)) \qquad (3)$$

In the second line of the above formula, the sum over $k_{\mathrm{L},z}$ on the initial side was replaced by the integral over $E_{\mathrm{L},z}$. $g_{\mathrm{L}}(E_z)$ is the corresponding density of states. As this review mainly deals with tunnelling processes between two two-dimensional systems, we now evaluate the matrix element M_{LR} for the case that both the initial and final states are purely two dimensional. As in a two-dimensional system, the states are quantized in the z direction but free motion of electrons exists in the x and y directions; the wavefunctions for the left- and right-hand sides are written as

$$\Psi_{\mathrm{L}} = \Psi_{\mathrm{L}}(z)\exp(\mathrm{i}k_{x,\mathrm{L}}x)\exp(\mathrm{i}k_{y,\mathrm{L}}y)$$

$$\Psi_{\mathrm{R}} = \Psi_{\mathrm{R}}(z)\exp(\mathrm{i}k_{x,\mathrm{R}}x)\exp(\mathrm{i}k_{y,\mathrm{R}}y). \qquad (4)$$

Inserting the wavefunctions into the expression for the matrix element and evaluating the integrals yields

$$M_{\mathrm{LR}} = -\frac{\hbar^2}{2m^*}\left(\Psi_{\mathrm{R}}^* \frac{\partial \Psi_{\mathrm{L}}}{\partial z}\bigg|_{z=z_0} - \Psi_{\mathrm{L}} \frac{\partial \Psi_{\mathrm{R}}^*}{\partial z}\bigg|_{z=z_0} \right) \times \delta(k_{x,\mathrm{L}} - k_{x,\mathrm{R}})\delta(k_{y,\mathrm{L}} - k_{y,\mathrm{R}}). \qquad (5)$$

The first term is simply the transmission coefficient of the barrier. The δ-functions are the evaluated overlap integrals of the wavefunctions in the x and y directions between the initial and final states. For 2D–2D tunnelling processes, these wavefunctions are plane waves on both sides of the barrier and the overlap integrals in the x and y directions yield δ-functions. This means that the wavevectors parallel to the barriers (k_x, k_y) have to be conserved for 2D–2D tunnelling processes.

3.2. 2D–2D tunnelling in the $B\|j$ configuration

We now investigate the influences of magnetic fields which are applied perpendicular to the sample. In this case, Landau levels are formed in the 2D systems on both sides of the barrier having quantization energies of $E_n = \hbar\omega_{\mathrm{c}}(n + 1/2)$. In Landau gauge, the corresponding wavefunctions can be expressed as

$$\Psi_{\mathrm{L}} = \Psi_{\mathrm{L}}(z)\exp(\mathrm{i}k_{x,\mathrm{L}}x)\Phi_{n,\mathrm{L}}(y)$$

$$\Psi_{\mathrm{R}} = \Psi_{\mathrm{R}}(z)\exp(\mathrm{i}k_{x,\mathrm{R}}x)\Phi_{m,\mathrm{R}}(y). \qquad (6)$$

m and n denote different Landau level indices on each side of the barrier. The matrix element is written as

$$M_{\mathrm{LR}} = -\frac{\hbar^2}{2m^*}\left(\Psi_{\mathrm{R}}^* \frac{\partial \Psi_{\mathrm{L}}}{\partial z}\bigg|_{z=z_0} - \Psi_{\mathrm{L}} \frac{\partial \Psi_{\mathrm{R}}^*}{\partial z}\bigg|_{z=z_0} \right) \times \delta(k_{x,\mathrm{L}} - k_{x,\mathrm{R}}) \int \Phi_{m,\mathrm{L}}(y)\Phi_{n,\mathrm{R}}(y)\,\mathrm{d}y. \qquad (7)$$

This expression is similar to equation (5), since it still contains the identical expression for the transmission coefficient and the δ-function for k_x conservation. For the y direction, however, the matrix element now contains the overlap integral between the Landau levels on each side of the barrier. It must be pointed out that due to the orthogonality of the harmonic oscillator states this overlap integral is zero for different Landau level indices. Thus transitions are only possible between states of the same index $m = n$. Due to scattering processes and imperfections of the sample, however, the forbidden transitions are nevertheless observed as weak structures in the tunnelling current or its derivative.

3.3. 2D–1D tunnelling

Also transitions between states of different dimensionality can be treated in terms of the transfer Hamiltonian formalism. We first look at transitions between a 2D system and a quantum wire. The wavefunctions are plane waves in the x and y directions on the 2D side. For the quantum wire side, we have plane waves in the x direction and quantized states in the y direction. Thus the wavefunctions are written as

$$\Psi_{\mathrm{L}} = \Psi_{\mathrm{L}}(z)\exp(\mathrm{i}k_{x,\mathrm{L}}x)\exp(\mathrm{i}k_{y,\mathrm{L}}y)$$

$$\Psi_{\mathrm{R}} = \Psi_{\mathrm{R}}(z)\exp(\mathrm{i}k_{x,\mathrm{R}}x)\Phi_{n,\mathrm{R}}(y). \qquad (8)$$

The matrix element for the 2D–1D tunnelling process is

$$M_{\mathrm{LR}} = -\frac{\hbar^2}{2m^*}\left(\Psi_{\mathrm{R}}^* \frac{\partial \Psi_{\mathrm{L}}}{\partial z}\bigg|_{z=z_0} - \Psi_{\mathrm{L}} \frac{\partial \Psi_{\mathrm{R}}^*}{\partial z}\bigg|_{z=z_0} \right) \times \delta(k_{x,\mathrm{L}} - k_{x,\mathrm{R}}) \int \exp(\mathrm{i}k_{y,\mathrm{L}}y)\Phi_{n,\mathrm{R}}(y)\,\mathrm{d}y. \qquad (9)$$

As one can see, the 2D–1D tunnelling process looks similar to the case of magnetic fields. Still, the momentum in the x direction is conserved. The overlap integral between the

plane waves on the 2D side and the quantized state in the y direction in the quantum wire, however, is remarkable: the overlap integral between the plane wave of the initial state and the 1D final state is simply the Fourier transform of the wavefunction of the 1D state. We now assume that the 2D systems are shifted in energy by eV_b with respect to each other. Total energy conservation requires that

$$E_{n,L} + \frac{\hbar^2 k_{x,L}^2}{2m^*} + \frac{\hbar^2 k_{y,L}^2}{2m^*} + eV = E_{\mu,R} + \frac{\hbar^2 k_{x,R}^2}{2m^*}. \quad (10)$$

As we can ignore the free motion in the x direction, this equation can be expressed in terms of k_y:

$$k_y(V) = \pm\sqrt{\frac{2m^*}{\hbar^2}(E_{\mu,R} - E_{n,L} - eV)}. \quad (11)$$

This means that the wavevector of the tunnelling electron, k_y, is controlled by the external voltage, and thus the measured current–voltage characteristics directly correspond to the Fourier transform of the wavefunctions in the 1D state.

3.4. 2D–0D tunnelling

For 2D–0D transitions the situation is similar, but for simplicity a cylindrical coordinate system is used to describe the electronic properties of the 0D system. The wavefunctions are therefore characterized by a function $\Psi_A^{0D}(\boldsymbol{\rho}, \varphi, z; n_A, m_A)$, where n_A represents the radial and m_A the azimuthal quantum number. As the unstructured accumulation layer (index A) exhibits only one subband, these two quantum numbers are sufficient to describe the 0D states in the MQD system. The wavefunctions of the subbands in the inversion layer (index I) are given by $\Psi_{I,\nu}^{2D}(\boldsymbol{\rho}, \varphi, z; m_I)$. Here ν stands for the 2D subband index, m_I takes the degeneration of $E_\parallel$ (energy of the motion parallel to the interface) into account. As coupling between the coordinates is neglected, it is possible to use the following separation ansatz

$$\begin{aligned} \text{2DEG: } \Psi_{I,\nu}^{2D} &= \frac{1}{\sqrt{A_{\rho\varphi}}}\Psi_{I,\nu}(z)\frac{1}{\sqrt{2\pi}}\exp(\mathrm{i}m_I\varphi)J_{m_I}(k_\parallel\rho) \\ \text{0DEG: } \Psi_A^{0D} &= \frac{1}{\sqrt{A_{\rho\varphi}}}\Psi_A(z)\frac{1}{\sqrt{2\pi}}\exp(\mathrm{i}m_A\varphi)\phi_{n_A,m_A}(\rho). \end{aligned} \quad (12)$$

The area $A_{\rho\varphi}$ represents the normalization constant in both systems. The matrix element $|M_{AI}|^2$ which is governed by the overlap of the single wavefunctions can be obtained by the following expression

$$\begin{aligned} M_{AI} &= \frac{-\hbar^2}{2m^*}\int\!\!\int_S \mathrm{d}x\,\mathrm{d}y\left(\Psi_I^*\frac{\partial\Psi_A}{\partial z} - \Psi_A\frac{\partial\Psi_I^*}{\partial z}\right) \\ &= \underbrace{\frac{-\hbar^2}{2m^*}\left(\Psi_{I,\nu}^*\frac{\partial\Psi_A}{\partial z} - \Psi_A\frac{\partial\Psi_{I,\nu}^*}{\partial z}\right)_{z=z_b}}_{t_B}\delta_{mI,m_A} \\ &\quad\times\underbrace{\int \mathrm{d}\rho\,\rho J_{m_I}(k_\parallel\rho)\phi_{n_A,m_A}(\rho)}_{\langle J_m(k_\parallel\rho)|\phi_{n_A,m}(\rho)\rangle}. \end{aligned} \quad (13)$$

The first term in this equation, t_B, represents the transmission coefficient of a single-barrier heterostructure. The δ-function in the middle of equation (13) guarantees the conservation of the angular momentum (quantum number m) during the tunnelling process. For the matrix element non-zero values can only be obtained for $m_I = m_A \equiv m$.

The value of the corresponding matrix element is a function of the radial quantum number n_A, the (common) azimuthal quantum number m, and the wavevector $\boldsymbol{k}_\parallel$ which depends on the applied bias voltage. Its value, however, is fixed by demanding the conservation of the total energy (10)

$$\tilde{k}_\parallel(V_b) = \sqrt{\frac{2m^*}{\hbar^2}(E_{n_A,m} - E_{\nu_I} - eV_b)}. \quad (14)$$

Thus, for 2D–0D tunnelling processes as well, all structure in the resonant tunnelling current will be caused by the behaviour of the overlap matrix element $I_{n_A,m}$ as a function of bias voltage. Further, the calculations have shown that the value of the overlap matrix element $I_{n_A,m}$ not only depends on the quantum numbers n_A and m and on the bias voltage V_b, but also on the particular potential profile, which will be demonstrated later in this review.

Going back to the expression for the tunnelling current (equation (3)), one can see that the tunnelling current is controlled by four components: the density of states, the transmission coefficient of the barrier, the overlap integral and the distribution function. As tunnelling experiments are always performed at very low temperatures, the influence of the distribution function can normally be ignored. It is shown below that in all experiments the observed structures in the tunnelling current are due to the influence of the transmission coefficient, the density of states or the wavefunction overlap between the initial or final states and for 1D–2D and 2D–0D tunnelling the experimental results are quantitatively analysed in terms of the transfer Hamiltonian formalism.

4. 2D–2D tunnelling experiments in zero magnetic field

An effect which is mainly controlled by the transmission coefficient of double-barrier structures is the height of the resonance peak on double-barrier resonant tunnelling diodes and the corresponding ratio between the maximum current in resonance and the minimum current ('valley current') at off-resonance conditions. Experimentally, it has been found that a two-dimensional emitter improves this peak to valley ratio, and thus different ways to establish such a two-dimensional emitter have been explored. On GaAs–AlGaAs double-barrier diodes, a two-dimensional emitter is formed under bias on samples having an undoped GaAs region in front of the barriers. Such samples exhibit good peak to valley ratios but not very high current densities, which is related to the series resistance caused by the undoped regions. On InGaAs double-barrier structures, however, a two-dimensional emitter can be realized as an InAs pre-well, which provides both high current densities

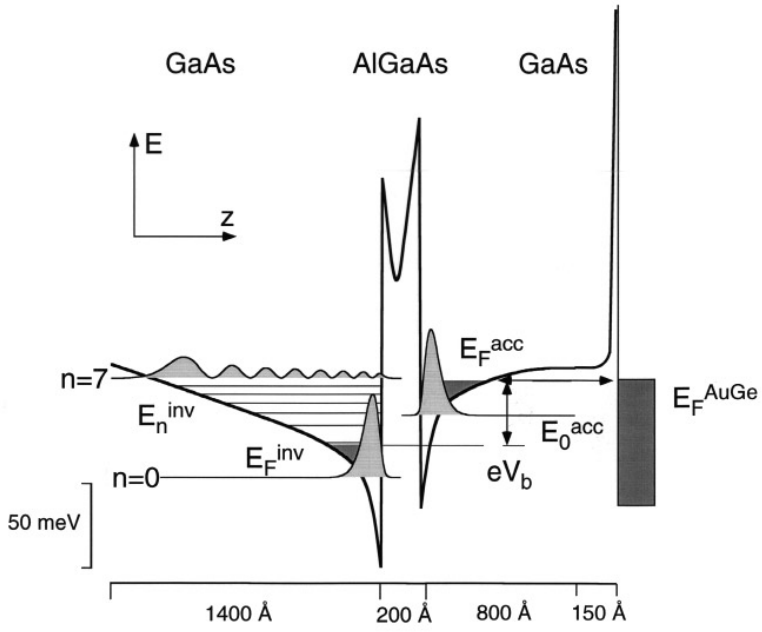

Figure 2. Self-consistently calculated conduction band profile at a bias voltage V_b. E_n^{inv} and E_0^{acc} denote the subband energies in the inversion and accumulation layers. E_F^{inv} and E_F^{acc} are the corresponding Fermi energies. E_F^{AuGe} is the Fermi energy in the top AuGe electrode and V_b the applied bias voltage.

and good peak to valley ratios. These features are most important for device applications [45, 46].

Density of state effects in the initial and final electrodes, however, are mainly responsible for all resonant transitions between two-dimensional systems. The first tunnelling processes between two purely two-dimensional systems were reported by Smoliner *et al* [47, 48]. The samples for these experiments consist of an unintentionally p-doped GaAs layer grown on a semi-insulating substrate followed by an undoped spacer ($d = 50$ Å), doped $Al_xGa_{1-x}As$ ($d = 50$ Å, $N_D = 3 \times 10^{18}$ cm^{-3}, $x = 35\%$), another spacer ($d = 100$ Å) and n-doped GaAs ($d = 800$ Å, $N_D = 1.2 \times 10^{15}$ cm^{-3}. The additional GaAs cap layer was highly n-doped ($d = 150$ Å, $N_D = 6.2 \times 10^{18}$ cm^{-3}). A self-consistently calculated conduction band profile is shown in figure 2. One can see that two 2D electron systems are formed on both sides of the doped barrier. The lower 2D gas in the undoped GaAs is an inversion layer with one occupied subband and several empty higher subbands; the upper 2D gas in the n-GaAs is an accumulation layer with one occupied subband. Higher empty states do not exist on the n-doped side, since they are already located above the GaAs bandedge. Typical electron concentrations in the inversion and accumulation layer at liquid-helium temperature are $n^{inv} = 6.3 \times 10^{11}$ cm^{-2} and $n^{acc} = 5.7 \times 10^{11}$ cm^{-2}. The electron mobility at the upper interface is $\mu^{acc} = 35\,000$ cm^2 V^{-1} s^{-1} and $\mu^{inv} = 130\,000$ cm^2 V^{-1} s^{-1} in the lower channel. Although these 2D systems are only separated by a barrier of 200 Å, independent contacts to both channels can be fabricated as follows. First, ohmic contacts to both 2D channels are aligned using a AuGe alloy. To establish the tunnelling contact, an AuGe film is slightly diffused into the upper GaAs layers. Finally, the GaAs around the top contact is removed selectively, yielding independent contacts to both 2D channels.

Through the independent contacts, it is now possible to shift the 2D electron systems energetically with respect to each other so that the transitions between the different 2D subbands on each side of the barrier can be studied. These transitions are directly evident as peaks in the tunnelling current and its derivative. Such measurements are performed using a four-terminal conduction bridge [49], to compensate series resistances and to achieve a high resolution. This technique is crucial at strong magnetic fields, where the series resistances in the lower 2D channel become an oscillatory function of the magnetic field. As a further advantage of this system it was found, that to an extremely good approximation, all of the applied voltage drops over the barrier [50], so that the relative energy shift of the 2D systems in good approximation is equal to $e\Delta V$ and thus it is easy to determine the subband energy spacings in the 2D systems. The measurement of the subband spacings in the lower channels offers the possibility of determining the local impurity concentration in the GaAs buffer layer, which is an extremely important parameter for MBE growth.

To determine the local concentration of charged impurities in the GaAs buffered layer, the resonance positions in the tunnelling current were measured and then compared with self-consistent calculations. A typical $I(V_b)$ curve and its derivative is shown in figure 3.

The large number of sharp subband resonances reflects the high quality of the sample, especially the low background impurity concentration in the GaAs buffer layer. As the wavefunctions of the 2D subbands penetrate deeper into the GaAs with increasing subband index (see figure 2), a high-resolution measurement of the

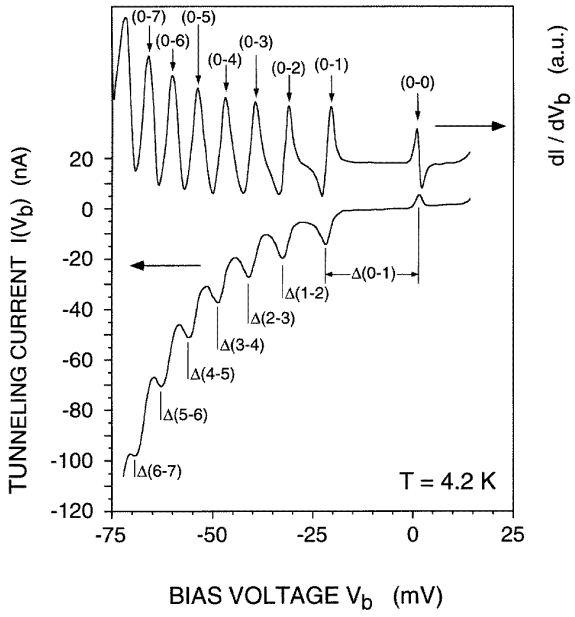

Figure 3. Typical $I(V_b)$ and dI/dV_b curves traced at 0 T and $T = 4.2$ K.

$I(V_b)$ peak positions in the tunnelling characteristics and the corresponding subband spacings offers the possibility for a depth-dependence determination of the impurity concentration in the uppermost region of GaAs buffer layer. Using the impurity concentration in the GaAs buffer as a fitting parameter, the background doping in the GaAs is obtained through a comparison of the calculated resonance positions with the measured peak positions in the tunnelling characteristics. To solve the Schrödinger equation, a one-dimensional finite difference method was applied, leading to an eigenvalue problem solved by EISPACK routines [51]. This method yields correct and stable solutions even in the case of relatively thick barriers such as those on the investigated sample. In analogy to the calculations performed by Stern and Das Sarma [52], non-parabolicity effects were also included in the calculation of the Hartree potential. Exchange and correlation effects [53] were also taken into account. Further details of this procedure have been published elsewhere [22, 54].

The best fit between experimental data and calculated impurity concentration in the GaAs buffer can be obtained if an exponentially decreasing impurity concentration in growth direction superimposed on a constant background is assumed. The result of this calculation is shown in figure 4, where the impurity concentration in the buffer layer is plotted as a function of the distance from the GaAs–AlGaAs interface (bold line). The thin lines indicate the range of the experimental error. In the considered range, the fit yields an exponential decrease of the impurity concentration from $N_A = 1.22 \times 10^{14}$ to 0.75×10^{14} cm^{-3} at the interface, according to the relation $N_A = [0.25 + 0.5\exp(-z/1800)] \times 10^{14}$ cm^{-3}, where z is measured in Å. This result indicates that the impurity concentration on top of the 2 μm thick GaAs buffer is still limited by the decay of the initial impurity concentration on the substrate surface and not by the saturation value of 0.25×10^{14} cm^{-3},

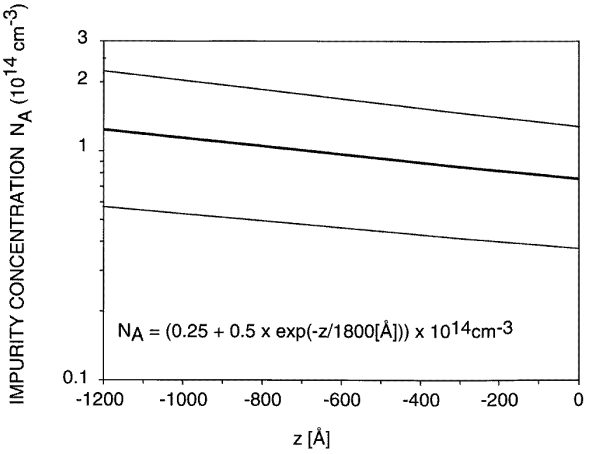

Figure 4. Background impurity concentration as a function of the distance from the GaAs–AlGaAs interface, which is located at $z = 0$.

which is a measure for the MBE machine inherent level of background doping.

Note that Hall measurements at such low doping levels encounter severe difficulties. A Hall measurement carried out on a equivalent bulk-like epitaxial layer with a thickness of 2 μm and a doping below 1×10^{15} cm^{-3} yields unreliable results or even fails, since the upper parts of the buffer or even the whole layer are surface depleted. If a sufficiently thick epitaxial layer is grown, for example for test purposes, one is not able to determine the concentration in the uppermost regions and, further, the impurity concentration will be different from the impurity concentration in a 'real' heterostructure.

5. 2D–2D tunnelling experiments in strong magnetic fields ($B \| j$)

In this section of the review we focus on the results obtained by so-called 'equilibrium tunnelling spectroscopy' in high magnetic fields. 'Equilibrium tunnelling spectroscopy' means that the experiments are performed between two 2D electron systems of equal densities at zero bias. Further, the Fermi energies are aligned at zero bias and the measurements are only carried out with high resolution in a small voltage range around $V_b = 0$. Thus, only transitions close to the Fermi energy are investigated. For all experiments, the orientation of the magnetic field is perpendicular to the layers of the sample, i.e. parallel to the tunnelling current.

The first measurements using equilibrium tunnelling spectroscopy were performed by Eisenstein *et al* [55, 56]. Later, similar experimental results were also obtained by Brown and co-workers [57]. The samples employed for these measurements are double quantum wells where one 2D subband is occupied in each well. The wells are embedded between AlGaAs layers having an aluminium concentration of approximately 30%. For all reported experiments, the wells are typically 200 Å wide and separated by a barrier of 175 Å or larger. The electron concentration in both wells are chosen in such a way that

the average distance between the electrons is of the order of the barrier thickness. Under this condition, interactions between the two 2D systems can be expected. If the fractional quantum Hall regime has to be investigated, the electron densities have to be low and the low-temperature mobilities have to be high ($n_s = 1.6 \times 10^{11}$ cm^{-2}, $\mu = 3 \times 10^6$ cm^2 V^{-1} s^{-1} [55]). Outside the fractional quantum Hall effect regime, electron densities around 3×10^{11} cm^{-2} and mobilities of $\mu = 8 \times 10^5$ cm^2 V^{-1} s^{-1} are also sufficient [57] to observe interactions between the 2D systems. It should be mentioned that for all experiments the density was adjusted to be the same in both 2D channels through additional backgate voltages.

For the above double quantum well structure, the tunnelling current was measured without and also in strong magnetic fields. As a main result it was found that in contrast to the $B = 0$ T the resonant tunnelling current is suppressed around zero bias for high magnetic fields. The onset of the tunnelling current is clearly at bias voltages larger than 0 V, followed by a large resonance peak. It must be pointed out that these effects were only observed for a magnetic field regime, where the Landau level filling factor is less than 1. The current onset and the peak position shift to higher voltages was also observed and explained by tunnelling processes into the first excited Landau level.

The qualitative explanation for the strong suppression of the tunnelling current around zero bias lies in the strongly correlated nature of the 2D electron gas in the lowest Landau level. The magnetic field localized the electrons on the scale of the magnetic length, and at sufficiently high fields a Wigner crystallization occurs [58] in both 2D channels of the sample. An electron tunnelling between the strongly correlated systems must first be extracted from the emitter and then be injected into an interstitial position of the Wigner crystal in the final electrode. The additional energy which is necessary to inject the electron into the Wigner crystal, and also the energy to eject the electron from the Wigner crystal in the emitter electrode, suppresses tunnelling around the Fermi level and thus a pseudogap is generated. A quantitative explanation of this effect, including the influence of magnetophonons and magnetoplasmons, which are generated when an electron is injected into the Wigner crystal, is given in [59]. Note that this gap at the Fermi energy can also be observed in 3D–2D tunnelling experiments, where electrons tunnel from a doped bulk region into a quantum well [60]. Using intensive temperature studies of the magnetic field-dependent tunnelling conductance, this work made localization effects responsible for the observed effects.

The latest studies on the above double quantum well structure even show evidence of an interlayer exciton in the tunnelling of electrons between both 2D systems [61]. The idea behind this is that a tunnelling electron leaves a hole in the emitter electrode. Owing to the high amount of correlation, this strongly localized charge defect has a relatively long lifetime and results in changes of the energy gap between the quantum wells for different barrier widths.

Besides direct tunnelling measurements, another topic of interest is the influence of a second 2D electron system on the quantum Hall effect and fractional quantum Hall effect [29]. For this purpose, magnetotransport experiments were carried out on the above double-layer 2D electron system. It was found that two new states exist in such a sample at filling factors of $\nu = 1$ and $\nu = 0.5$. Studies of samples with different densities and layer separations and also experiments with in-plane magnetic fields were used to show that these two states arise from an interplay between intra- and interlayer Coulomb interactions. This influence of the fractional quantum Hall effect can also be observed in double-barrier diodes with a two-dimensional emitter [62].

On the double-heterostructure sample, the additional magnetic field causes Landau levels in both 2D systems, which are equally spaced by $\hbar\omega_C$ (ω_C is the cyclotron frequency), and thus extra structures in the tunnelling current can be expected due to transitions between barrier-separated Landau levels. In 1970, Tsui [3] investigated the Landau level spectra in narrow accumulation channels using tunnelling spectroscopy. Oscillations in the second derivative of the tunnelling current were observed as a result of the Landau levels in the accumulation channel, which give a direct measure of the in-plane effective mass of the confined electrons. Since then, many magnetotunnelling experiments have been performed on single-barrier [63] and double-barrier [64, 65] heterostructures. In the latter case, tunnelling through Landau levels inside the well was also observed. More recently, Kane *et al* [66] found evidence for inter-Landau level tunnelling in a 2DEG between regions of different electron concentrations induced by a gate contact. When a magnetic field was applied, the current between the two regions of different electron densities showed a backward pn-diode-like behaviour. Treating the Landau level separation at the boundaries of the two regions of different electron densities as similar to the bandgap of a semiconductor diode, the existence of inter-Landau level tunnelling was used to explain the current flow under reverse bias.

In double heterostructures, however, the situation is somewhat different as well defined Landau levels exist both in the inversion channel and in the accumulation layer, which are only 200 Å apart. The total energy of the electrons, for example in the inversion layer, is therefore given by $E = E^{\mathrm{inv}}_{n,N} = E^{\mathrm{inv}}_n + \hbar\omega_c(N + 1/2)$. If an electron that tunnels from the accumulation into the inversion layer suffers no scattering during the tunnelling process, the momentum and energy parallel to the barrier are conserved and thus a conservation of the Landau level index is expected. If the applied bias voltage adjusts two subbands energetically into resonance position, all Landau levels on both sides of the barrier are aligned automatically, as their spacing is only determined by the magnetic field. Shifting the quantized systems by $\hbar\omega_c$ with respect to each other, a situation is generated where two Landau levels of different index are aligned. As the Landau level index has to be conserved during the tunnelling process, such a transition is forbidden in the absence of scattering, and therefore no extra structures in the tunnelling current can be expected. Due to the non-ideal situation in 'real' samples, however, a certain number of scattering events can take place during the tunnelling process. Consequently,

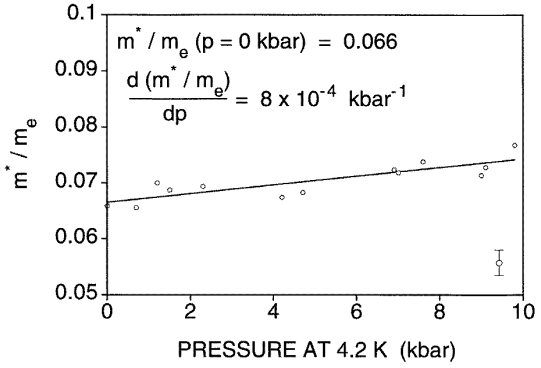

Figure 5. GaAs effective mass as a function of hydrostatic pressure.

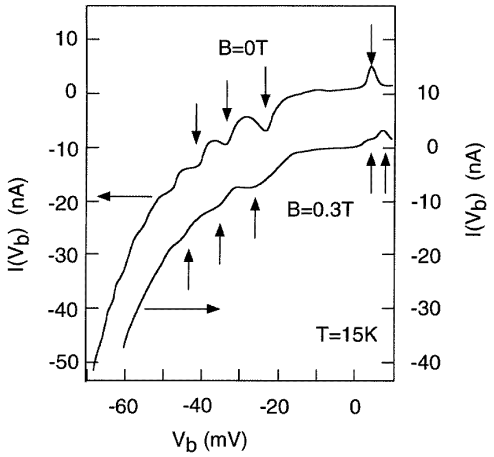

Figure 6. $I(V_b)$ curves traced at B = 0 T and at an in-plane magnetic field of B = 0.3 T.

normally forbidden transitions between Landau levels of different index [67] are also evident as a series of extra structures in the derivative of the tunnelling characteristics. These extra peaks are spaced by $\hbar\omega_c = eB/m^*$, where m^* is the effective mass of electrons. Measuring the magnetic-field-dependence peak positions with high resolution, the GaAs effective mass, and also its dependence on external hydrostatic pressure, can be determined [68] (see figure 5).

6. 2D–2D tunnelling in the $B \perp j$ configuration

Tunnelling in a configuration where the magnetic field is applied parallel to the layers of the sample and perpendicular to the direction of the tunnelling current ($B \perp j$) has been performed on different structures by several groups during the last few years. The most common configuration is the double-barrier heterostructure, which consists of two barriers with a quantum well in between. The electrodes on both sides of the structure are of three-dimensional character, whereas the motion of the electrons is completely quantized inside the well, where a two-dimensional electron gas (2DEG) is formed between the barriers. Results on this system have been reported for GaAs/AlGaAs [69–72] and InP/InGaAs [73] heterostructures. Similar experiments have also been performed on barrier-separated superlattices [74]. In single-barrier structures, tunnelling is observed between the two sets of states on both sides of the barrier, where the dependence of the transmission probability on the energy can be neglected. With applied in-plane magnetic fields, the features in the $I(V_b)$ characteristic broaden significantly and are observed to shift to higher energies. More recently, attention has focused on the valence band. In the AlAs/GaAs system [75], a double-barrier configuration was used to study the valence subbands in the central quantum well, where in this case the emitter was of two-dimensional character. For the Si/SiGe system [76, 77], tunnelling in in-plane magnetic fields has been used to study in-plane effective masses of the valence subbands, and angular ansitropy. In contrast to optical measurements, which tend to average over k space, magnetotunnelling spectroscopy allows the investigation of specific k-values, because energy and momentum must be conserved in the resonant tunnelling process. Thus, only particles eligible for tunnelling contribute to the resonant current, and the dependence of the resonance peak position and its shape on in-plane magnetic fields yields information on the band structure.

For a double quantum well structure, 2D–2D tunnelling processes have been investigated using a double quantum well structure with strongly different mobilities. On such a sample, the in-plane sample resistance exhibits a maximum when the structure is driven into resonance. This effect is explained by the fact that, in resonance, the 2D state on the high-mobility side is extended to the low-mobility side and therefore suffers more scattering. In sufficiently high magnetic fields applied parallel to the layers of the sample, however, this resistance maximum can be quenched [78]. Here, the in-plane magnetic field causes a deformation of the wavefunction and Fermi surfaces, so that the coupling of the wavefunctions in both 2D channels is suppressed in resonance.

On the 2D–2D double-heterostructure structure, an interesting influence of small in-plane magnetic fields on the $I(V_b)$ curves is shown in figure 6. Here, the resonant features show different behaviour with applied in-plane magnetic fields, depending on whether both or just one of the subbands involved in the transition are occupied by electrons. In the first case, the resonant peak at $B = 0$ T splits into two peaks, which shift to higher/lower energies when the magnetic field is increased. When the target subband is empty, the resonant feature shifts to higher energy, and exhibits a characteristic 'shoulder'. In addition, resonance broadening takes place. By comparison with computer-simulated $I(V_b)$ curves it is shown that this behaviour of the resonant features under in-plane magnetic fields is due to a difference in effective mass between the initial and final states, which occurs since they are different in energy. Figure 7 shows this influence of the non-parabolicity as a function of energy [79].

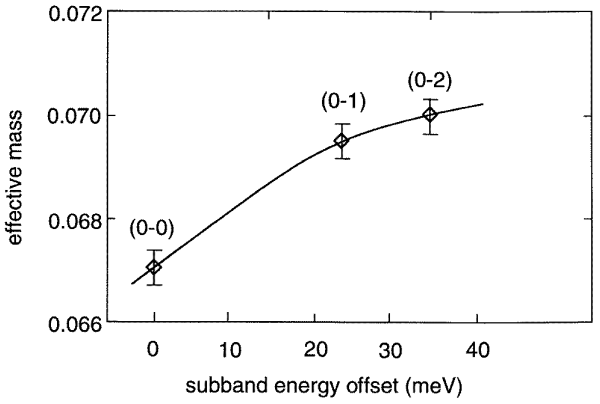

Figure 7. GaAs effective mass as a function of energy.

7. Tunnelling between 2D and lower-dimensional systems

In this section, transitions between 2D systems and electron systems of lower (1D, 0D) different dimensionality are discussed. Taking double-barrier resonant tunnelling diodes as a starting point, epitaxial regrowth techniques either on V-groove etched substrates, as proposed by Luryi and Capasso [80], or on the edge of *in situ* cleaved substrates [81] lead to devices where electrons tunnel resonantly from a 2D emitter state into 1D wire subbands [82]. In this geometry, tunnelling proceeds from the edge of a two-dimensional electron source through the bound state in a quantum wire into the edge of a 2D electron system. The mixing of the longitudinal and perpendicular motion of the carriers allows a detection of the wire's states of excited perpendicular motion in such a sample. For double-barrier resonant tunnelling diodes, the lateral motion can also be restricted by use of focused Ga ion-beam implantation [83]. In that experiment, effects of mixing 2D emitter subbands with 1D subbands in the double-barrier region could be observed, which are related to their particular parity [84]. In theoretical models, subband mixing and coupling effects turned out to be important and have to be taken into account [85, 86].

In contrast to vertical tunnelling geometries, lateral 1D to 2D tunnelling geometry can also be implanted on modulation-doped field effect transistor heterostructures by using electron-beam lithography [87] where the 1D density of states is reflected in the tunnelling current. For this experiment, a splitgate geometry with a 'leaky' 1D channel is used. In this leaky 1D system, electrons can tunnel out of the 1D channel through a thin sidewall barrier into an adjacent 2D electron bath [88]. A sharp peak and a valley structure can be observed in the 1D–2D tunnelling current, when the carrier concentration in the 1D channel is modulated through the splitgates. These structures are due to the influence of the subbands in the 1D channel, and in addition it was shown that electron waveguiding exists in this system, which is completely independent of the observation of conductance quantization.

On the double 2D heterostructure, 1D–2D tunnelling can be realized if the upper channel is structured into quantum wires by laser holography [89]. In this case, tunnelling processes between a multiple quantum wire (MQW) system and a 2DEG can be investigated. It must be pointed out that in this geometry both the initial and the final states involved in a tunnelling transition are quantized in such a way that no free momentum component exists in the direction of the tunnelling current. Under these conditions, the tunnelling probability and selection rules turn out to depend strongly on the profile of the confining potential and therefore on the shape of the one-dimensional (1D) wavefunction. In order to illustrate this effect, a transfer Hamiltonian formalism was used to calculate the transition probability for quantum wire potentials of different shape. In the case of a square well potential, no additional resonance structures (if compared to tunnelling between two 2DEGs) are to be expected. For a smooth cosine-shaped potential, however, all 1D states give rise to a multitude of resonant structures in the tunnelling current. From the experimental results it was concluded that in the investigated MQW system the potential can qualitatively be best described by a harmonic oscillator-like profile. In addition, the temperature behaviour of the resonance structures caused by the 1D states was studied both experimentally and theoretically, yielding quantization energies in the quantum wires. If the thermal energy exceeds the 1D subband spacing, significant changes of the 1D potential, caused by the occupation of higher subbands and reduced screening effects, have to be taken into account.

Further structuring even allows us to study tunnelling processes between 2D and 0D states [90]. To obtain such samples, where electrons tunnel between a multiple quantum dot array and a 2DEG, holographic photoresist grids with a period of $a = 350$ nm were fabricated in the area of the tunnelling contact using a UV laser interference pattern and a double-exposure technique. In order to deplete the accumulation layer in the uncovered regions, the dots were wet chemically etched around 300 Å deep into the GaAs cap layers. The remaining islands have a diameter of $\approx a/2$, resulting in a three-dimensional confinement of the carriers in the accumulation layer. As earlier, AuGe was evaporated over the total area of the tunnelling contact, establishing ohmic contacts to the quantum dot system. As a result, one has a system where quantum wires and a 2DEG are independently contacted, although separated only by a barrier of 200 Å. The sample geometry is shown schematically in figure 8.

By applying a voltage V_b, the 0D states are shifted energetically by $\Delta E = e\Delta V_b$ with respect to the 2DEG, since this external electric field drops completely across the potential barrier. A negative bias voltage $V_b < 0$ corresponds to tunnelling processes from a 0D state of the MQD system into a 2D subband of the inversion channel. The bandstructure of the sample, which illustrates this situation, is shown in figure 8 for both the etched and the unetched regions (upper and lower part respectively).

The experimental results are plotted in figure 9. Figure 9(a) shows the dI/dV_b characteristics of the nanostructured 0D–2D sample, where the temperature is varied between $T = 1.7$ K (curve (1)) and $T =$

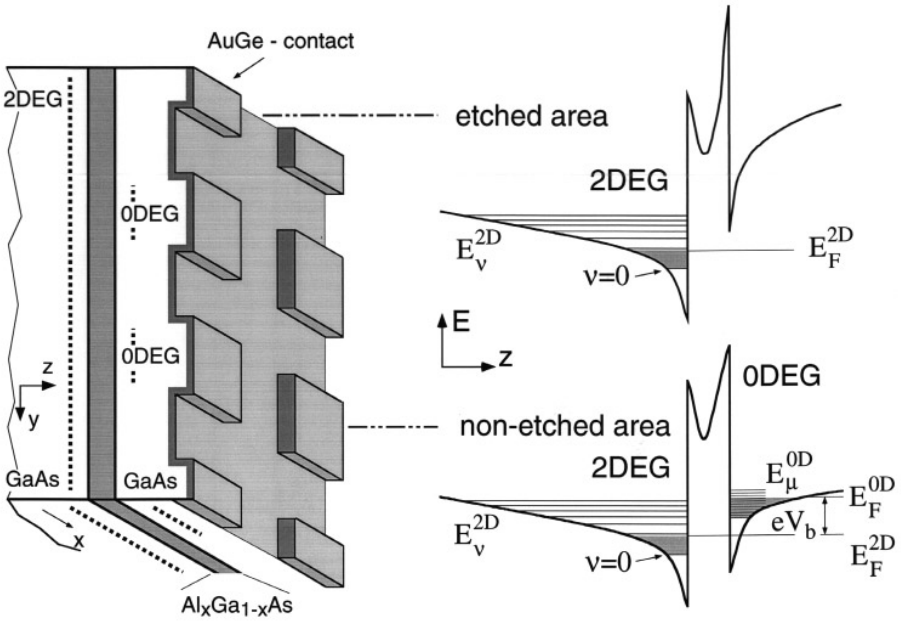

Figure 8. A schematic view of a 0D–2D sample is shown on the left-hand side. The corresponding conduction band profile for the etched and unetched areas of the sample is shown on the right.

40 K (curve (12)). For reference reasons, the $\mathrm{d}I/\mathrm{d}V_\mathrm{b}$ characteristics of a non-nanostructured sample are plotted in part (b) of figure 9 for the two temperature values $T =$ 1.7 K (curve (1)) and $T = 40$ K (curve (2)). A comparison of the two characteristics (curve (1) in (a)) and (curve (1) in (b)) shows that the nanofabrication process leads to a multitude of new resonances which exist within the whole voltage range considered. At small negative bias voltages in particular new resonance structures can be observed, in a regime where the characteristic (curve (1) part (b)) is absolutely flat. With regard to the amplitudes and the positions of the new peaks, there exists no obvious correlation between the 2D–2D and the 0D–2D tunnelling characteristic. Nevertheless it has to be stressed that all resonance structures are fully reproducible within the investigated bias voltage regime. All resonance peaks of the 0D–2D $\mathrm{d}I/\mathrm{d}V_\mathrm{b}$ characteristic, however, show a strong dependence on the temperature. Above $T = 4.2$ K (curve (2) part (a)), only about half of the resonances can still be resolved. A further increase of the temperature results in a monotonic broadening of all resonance structures, accompanied by a monotonic decrease of peak amplitudes. For bias voltages $V_\mathrm{b} < 0$, one can observe a common shift of all structures to more negative values of V_b, whereas the peak positions at positive bias voltage remain almost unchanged at temperatures $T >$ 4.2 K. The subband resonances of the 2D–2D $\mathrm{d}I/\mathrm{d}V_\mathrm{b}$ characteristic (curve (1) part (b)) behave in the same way. With rising temperature, the peak amplitudes decrease rapidly, whereas the linewidth increases simultaneously. The shift of these resonance structures is due to the thermally activated occupation of the first excited subband in the inversion channel which causes a self-consistent modification of the potential profile. In both parts (a) and (b) of figure 9 the positions of the 2D–2D subband resonances are marked by arrows. The comparison of the two high-temperature characteristics (curve (12) in (a) and curve (2) in (b)) shows that the positions of the still resolvable resonances correspond to each other.

As shown above, the structures in the measured tunnelling characteristics are mainly caused by the overlap integral between the initial and final states. However, the calculations have shown that the value of the overlap matrix element $I_{n_\mathrm{A},m}$ not only depends on the quantum numbers n_A and m and on the bias voltage V_b, but also on the particular potential profile. In order to analyse the influence of the shape of the confining potential on the probability for tunnelling processes between 0D and 2D states in the present structure, we first discuss the results for radial symmetric square well potential of finite height.

In figure 10 the wavefunction overlap integral is plotted as a function of bias voltage for the lowest four quantum numbers of $n_\mathrm{A} =$ 1–4. The overlap integral $I_{n_\mathrm{A},m}$ of the $n_\mathrm{A} = 0$ ground state shows only a sharp resonance structure at $V_\mathrm{b} = V_0$ for $m = 0$ (upper part of figure 10). In the regime $V_\mathrm{b} > V_0$ no resonant tunnelling process is allowed, since the total energy cannot be conserved during the transition. For $V_\mathrm{b} < V_0$, the value of $I_{0,0}$ drops exponentially towards zero within a certain voltage range. The functions $I_{0,m}(V_\mathrm{b})$ corresponding to the states with higher angular momentum quantum number ($m \geq$ 1) also show a maximum in this regime, although its linewidth increases and its intensity decreases drastically as m becomes larger. The overlap integrals of the radial quantum numbers $n_\mathrm{A} = 1, 2$ and 3 are also plotted in figure 10 for different values of m. In all cases, a sharp resonance structure can only be obtained for the particular $m = 0$ states. The structures which are due to higher values of m always occur at more positive bias voltages than for $m = 0$. In addition, all overlap integrals with

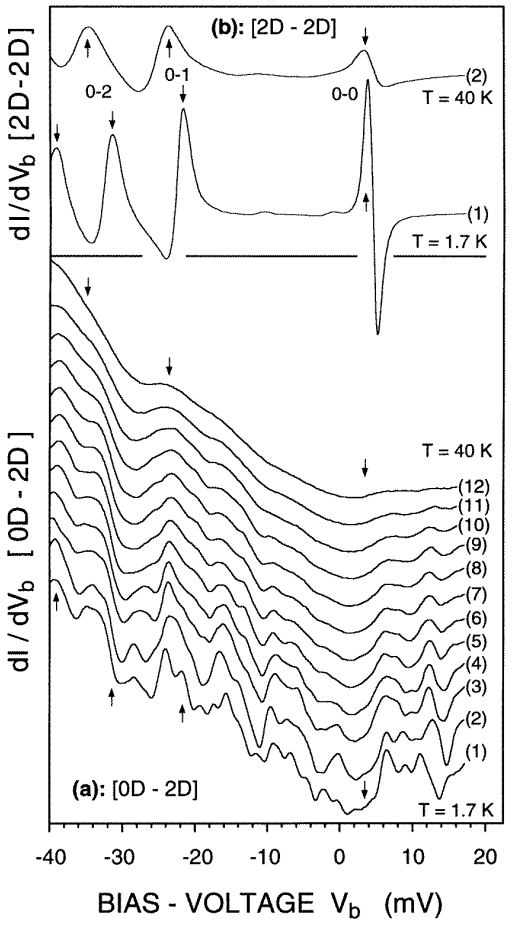

Figure 9. (a) Measured dI/dV_b curves in the temperature range between 1.7 K and 40 K. (b) For comparison, dI/dV_b curves of unstructured samples are also shown.

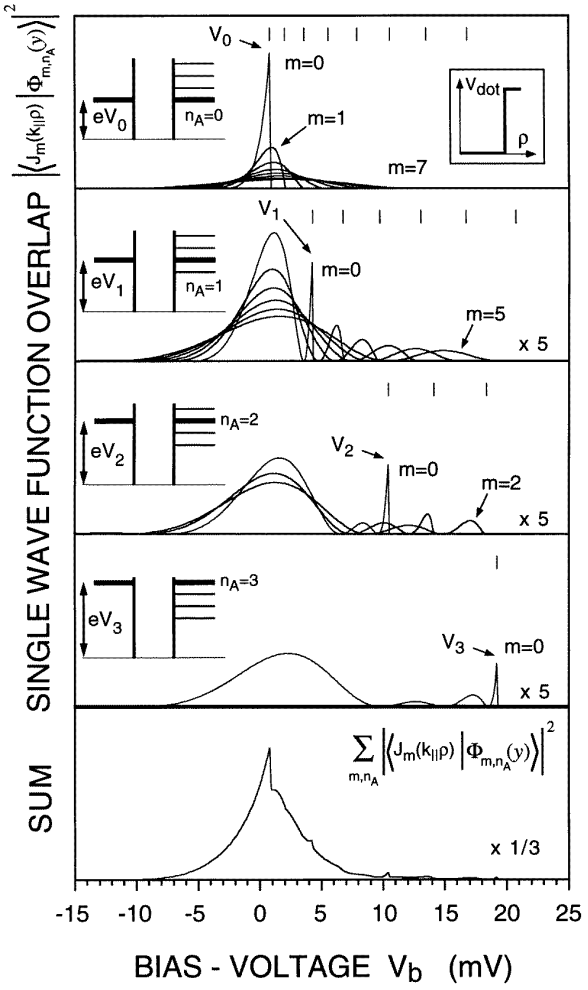

Figure 10. Calculated wavefunction overlap between the 2D state and the lowest three 0D states for a quantum dot with a rectangular potential of finite height. The sum over all 0D subbands is also shown.

larger n values ($m = 0$) have a large and relatively broad peak at the voltage position V_0.

To understand this behaviour, one has to start from equation (14). According to this equation, the wavevector $\boldsymbol{k}_\parallel$ of the tunnelling electrons is tuned by the applied bias voltage as all other parameters in this equation are constant. Analysing the peak positions ($m = 0$) quantitatively, one can see that each peak in the overlap integral is due to a situation where the expression $i\pi/k = w$ is equal to the width of the dot, w (i is an integer). In other words, peaks in the wavefunction overlap are always expected when a multiple integer of half of the wavelength of the tunnelling electron, $\lambda/2$, fits into the dot, where $k = 2\pi/\lambda$. Note that this explains why the resonance peak for the overlap between the lowest 0D and the 2D subband is not exactly at the position where the subbands are aligned, but at somewhat more negative bias voltages. Here, the voltage where the width of the dot is equal to $w = 1\pi/k$ simply corresponds to the zero-point energy in the dot.

In general, the transition probability of each (radial) 0D state exhibits many different sharp and also broad resonance structures which leads to a very complex total tunnelling probability, as one has to sum over all states in the relevant energy range. The lowest part of figure 10 shows the sum of all single-wavefunction overlap integrals $I_{n_A,m}(V_b)$ for the rectangular potential. The resonance structures caused by the $m = 0$ states can still be clearly resolved but all other maxima of $I_{n_A,m}(V_b)$, cannot be definitely assigned to a particular tunnelling process since they are too weak and contributions of too many 0D states interfere. However, all functions $I_{n_A,m}(V_b)$ have a finite value in the vicinity of $V_b \approx V_0$ where they contribute to the total tunnelling probability. This effect leads to a global maximum of $\sum I_{n_A,m}$ around the position of the 0D ground state resonance, which will become important when discussing the temperature behaviour of the experimental results.

In order to take a realistic potential situation into account, one can choose a cosine-shaped quantum dot potential profile with radial symmetry, which is analytically given by the following expression:

$$V_{\mathrm{dot}}(\rho) = V_{\mathrm{mod}}\left[\frac{1}{2} + \frac{1}{2}\cos\left(\frac{\pi}{R_{\mathrm{dot}}}(\rho - R_{\mathrm{dot}})\right)\right] \qquad (15)$$

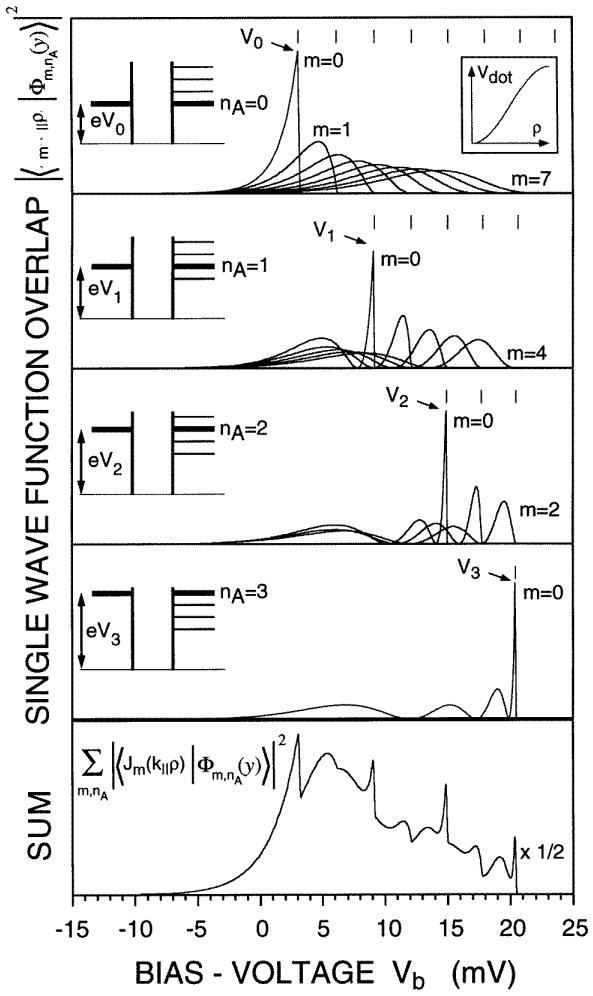

Figure 11. Calculated wavefunction overlap between the 2D state and the lowest three 0D states for a quantum dot with a cosine-shaped potential of finite height. The sum over all 0D subbands is also shown.

with $\rho \leq R_{\mathrm{dot}}$. The parameters for this model potential are chosen to obtain comparable quantization energies to those for the rectangular potential discussed above.

Figure 11 shows the results for this cosine-shaped potential, which can now be compared with the findings for the rectangular potential discussed above. At first glance, the shape of the overlap integrals is the same as for the rectangular potential, but somewhat broadened. If one looks at the peak positions for the overlap integrals of the higher subbands one can see two differences. First, the peaks are shifted with increasing subband index n, and second, the peak structure is much more pronounced, especially if one looks at the sum of the overlap integrals at the bottom of figure 11. The shift of the peaks is understood by the following arguments. As mentioned above, peaks in the wavefunction overlap are always expected each time $i\pi/k = w$. In a cosine-shaped potential the extension of the subbands increases with increasing subband index. This explains the shift of the peak positions to different bias voltages, which correspond to different k-values. The more pronounced peak structure is due to the different shape of

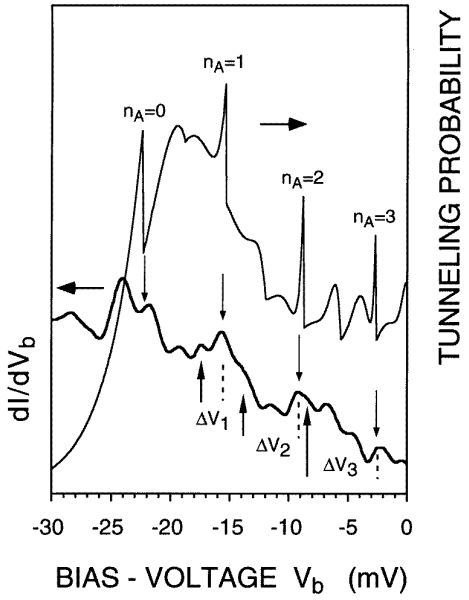

Figure 12. Comparison between the calculated tunnelling probability and the measured $\mathrm{d}I/\mathrm{d}V_{\mathrm{b}}$ curve at 1.7 K. The downward arrows mark the n = 0–3 resonance peaks. The upward arrows mark the i = 1 peak positions for each subband.

the wavefunctions in the cosine-shaped potential, since the overlap integral can be regarded as a Fourier transform of the quantum dot states. In a finite rectangular potential the wavefunctions are sinusoidal, which means that the Fourier transform of the wavefunction looks like a δ-function. For the cosine-shaped potential, the wavefunctions are roughly harmonic oscillator-like, which means that they contain 'higher frequencies' and the corresponding Fourier transform has a rich structure.

Figure 12 shows a comparison between the calculated tunnelling probability and the $\mathrm{d}I/\mathrm{d}V_{\mathrm{b}}$ curve measured at 1.7 K. As one can see, the experimental results agree well with the calculated peak positions obtained for a cosine-shaped model potential with $R_{\mathrm{Dot}} = 62.5$ nm and $V_{\mathrm{mod}} = 38$ meV. Not only the peak positions but also the larger modulation of the measured $\mathrm{d}I/\mathrm{d}V_{\mathrm{b}}$ curve are explained by the model. These larger maxima, on which the small peaks are superimposed, are due to contributions of many 0D states, which is consistent with the observed temperature behaviour of the peak amplitudes in $\mathrm{d}I/\mathrm{d}V_{\mathrm{b}}$. The small peaks smear out very quickly with increasing temperature, but the larger maxima stay clearly present up to $T \approx 15$ K since they are due to the interference of many 0D states. The weakly exponential background is not reproduced by the model calculation, since the transmission coefficient of the barrier was assumed to be constant for simplicity. Note that, strictly speaking, the calculated tunnelling probability has to be compared with the current–voltage characteristics. In $I(V_{\mathrm{b}})$, however, the structures are too weak to be resolved and thus, the comparison with $\mathrm{d}I/\mathrm{d}V_{\mathrm{b}}$ is justified.

Now the sharp structures in the total tunnelling probability which are due to the sharp peaks in the wavefunction overlap integrals for $n_{\mathrm{A}} = 0, 1, 2, 3$, are

assigned with single peaks in the tunnelling characteristics (marked in figure 12 with downward arrows) and determine the subband spacings between the lowest three 0D subbands in the quantum dot. If one takes into account that to a good approximation the relative energy shift of the 2D and 0D states is equal to $e\Delta V_b$, the subband spacings of the lowest three subbands are determined as $\Delta E_{01} \approx 7$ meV, $\Delta E_{12} \approx 6$ meV and $\Delta E_{23} \approx 5$ meV. These relatively high subband spacings are consistent with the parameters used for sample preparation, as the dots were etched rather deep into the GaAs on this sample. The decreasing subband spacings with increasing subband index clearly show that the potential in the dot is not rectangular or parabolic and that a cosine-shaped potential is the most realistic description of the situation.

It must be pointed out that nanostructuring is not always required to observe tunnelling processes between two-dimensional and low-dimensional systems. A good example is the work of Geim *et al* [91], who investigated transitions between a 2D electron gas in the emitter electrode of a double-barrier diode and donor states inside the well. These states can be regarded as strongly localized 0D states, and singularities in the tunnelling current can be observed when the emitter Fermi energy matches the energy of these localized states. Using the theoretical framework of Matveev and Larkin [92], this singularity was attributed to the Coulomb interaction between the fluctuating charge on the impurity site and the 2DEG. Similar investigations on tunnelling processes via localized 0D states were carried out by Hickmott, who investigated incoherent mesoscopic hole tunnelling through barrier states in p-type AlGaAs capacitors [93].

8. 1D–1D and 1D–0D tunnelling

Recent advances in microfabrication such as lithography, etching and epitaxial regrowth have made it possible to reduce the dimensions of semiconductor devices in such a way that 1D–1D and 1D–0D tunnelling processes can be studied. A vast amount of literature deals with single-electron effects such as the Coulomb blockade, which is normally investigated in double quantum dot structures realized by gates on high-mobility 2D systems. For more details on this topic see [94]. However, one has to keep in mind that these effects can also occur in asymmetric double-barrier resonant tunnelling diodes [95].

The first experiments on 1D–1D and 1D–0D tunnelling processes were carried out in ultra-small, pillar-shaped double-barrier resonant tunnelling diodes (DBRTDs) by Reed *et al* [96]. Resonance structures in the tunnelling current were assigned to resonant tunnelling processes between 1D states in the emitter region and the 0D states inside the quantum well defined by the two barriers [97]. In similar experiments, based on asymmetric DBRTDs, charge effects were also observed [95, 98]. Using a shallow etching process in combination with a sidegate, it is possible to adjust the 0D confinement by varying the gate voltage. The observed resonance structures in the tunnelling current through these devices were assigned to Coulomb blockade effects [99] as well as to ionized donor atoms [100]. Note that besides etching, focused ion beam implantation can also be used to define structures containing quantum dots [101]. Using triple-barrier RTDs as a starting point, tunnelling processes in coupled quantum dot structures have also been investigated experimentally [102] and theoretically [103, 104]. For these structures measurements have even been reported in transverse magnetic fields [105]. In most of the above experiments, a harmonic oscillator-shaped potential profile was used to describe the results. However, this turned out not always to be sufficient and thus an anharmonic oscillator model was introduced to simulate the experimental results [106]. In order to explain the fine structure of the current–voltage characteristics [107], further theoretical investigations of these tunnelling processes yielded a strong coupling between the 1D subbands in the contact region and the 0D states inside the quantum dots. However, sometimes the effect of the constriction geometry on quasi one-dimensional transport [108] cannot be neglected, and thus much effort has been made to investigate the influence of the dimensionality of the involved states with [109] magnetic fields and without magnetic fields [110, 111].

9. Summary

In summary it has been shown that tunnelling spectroscopy reveals a large number of interesting effects if the dimensionality of the states involved is reduced. A very instructive way to understand these experiments is to use the transfer Hamiltonian formalism. In terms of this formalism, all structures in the tunnelling current have their origin in density of states effects, transmission coefficients and the overlap integral between the initial and final states. As this formalism is not restricted to the dimensionality of the states involved, it can also be applied to tunnelling between systems of different dimensionality. Such transitions will become more and more important in future experiments, since advanced nanostructuring techniques allow the fabrication of 1D and 0D systems with high subband energies. For these systems the 1D and 0D quantum limit could be reached, which gives hope for a completely new class of experiments.

Acknowledgments

The author is grateful to E Gornik for continuous motivation, support and valuable discussions. W Demmerle, N Reinacher and G Rainer substantially contributed to this work. All samples were provided by G Böhm and G Weimann. This work was sponsored by Oesterreichische Nationalbank, project no 4874.

References

[1] Wolf L 1985 *Principles of Tunneling Spectroscopy* (New York: Oxford University Press)
[2] Tsui D C 1982 *Handbook of Semiconductors* vol 1, ed T W Moss and W Paul (Amsterdam: North Holland) p 662
[3] Tsui D C 1970 *Phys. Rev. Lett.* **24** 303

[4] Tsui D C 1971 *Phys. Rev.* B **4** 4438
[5] Tsui D C, Kaminski G and Schmidt P H 1974 *Phys. Rev.* B **9** 3524
[6] Pong-Fei Lu, Tsui D C and Cox H M 1984 *Appl. Phys. Lett.* **45** 772
[7] Kunze U 1984 *J. Phys. C: Solid State Phys.* **17** 5677
[8] Hickmott T W, Solomon P M, Fang F F, Stern F, Fisher R and Morkoc H 1984 *Phys. Rev. Lett.* **52** 2053
[9] Goldmann V J, Tsui D C and Cuningham J E 1987 *Phys. Rev.* B **36** 7635
[10] Pritchard R E, Harness P C, Cury L, Portal J C, Khamsehpour B, Truscott W S and Singer K E 1991 *Semicond. Sci. Technol.* **6** 626
[11] Leadbeater M L, Alves E S, Eaves E, Henini M, Hughes O H, Celeste A C and Portal J C 1989 *Superlatt. Microstruct.* **6** 63
[12] Nakagawa T, Imamoto H, Kojima T and Otha K 1989 *Appl. Phys. Lett.* **63** 2116
[13] Gobato Y G, Chevoir F, Berroir J M, Bois P, Guldner Y, Nagele J, Vieren J P and Vinter B 1991 *Phys. Rev.* B **43** 4843
[14] Cheng P and Harris J S Jr 1989 *Appl. Phys. Lett.* **55** 572
[15] Turley P J and Teitsworth S W 1994 *Phys. Rev.* B **50** 8423
[16] Mingo N, Porto J A and Sanchesz-Dehesa J 1994 *Phys. Rev.* B **50** 11 884
[17] Bang-Fen Zhu and Kun Huang 1993 *Phys. Rev.* B **48** 4575
[18] Mendez E E and Chang L L 1990 *Proc. 8th Int. Conf. on the Electronic Properties of Two-Dimensional Systems (Grenoble 1989) (Surf. Sci.* **229** 173) ed J Y Marzin, Y Gouldner and J C Maan
[19] Smoliner J, Gornik E and Weimann G 1988 *Appl. Phys. Lett.* **52** 2136
[20] Demmerle W, Smoliner J, Bethold G, Gornik E, Böhm G and Weimann G 1991 *Phys. Rev.* B **44** 3090
[21] Christanell R and Smoliner J 1988 *Rev. Sci. Instrum.* **59** 1290
[22] Reinacher N, Demmerle W, Smoliner J, Gornik E, Weimann G and Böhm G 1993 *J. Appl. Phys.* **74** 3593
[23] Eisenstein J P, Gramilla T J, Pfeiffer L N and West K 1991 *Phys. Rev.* B **44** 6511
[24] Eisenstein J P, Pfeiffer L N and West K W 1990 *Appl. Phys. Lett.* **57** 2324
[25] Eisenstein J P, Pfeiffer L N and West K W 1991 *Appl. Phys. Lett.* **58** 1497
[26] Linfield E H, Jones G A C, Ritchie D A and Thomson J H 1993 *Semicond. Sci. Technol.* **9** 415
[27] Brown K M *et al* 1994 *Appl. Phys. Lett.* **64** 1827
[28] Brown K M *et al* 1994 *J. Vac. Sci. Technol.* B **12** 1293
[29] Boebinger G S, Murphy S Q, Eisenstein J P, Pfeiffer L N, West K W and Song He 1994 *Surf. Sci.* **305** 8
[30] Song He, Xie X C, Das Sarma S and Zhang F C 1991 *Phys. Rev. Lett.* B **43** 9339
[31] Boebinger G S, Jiang H W, Pfeiffer L N and West K W 1990 *Phys. Rev. Lett.* **64** 1793
[32] Harris J J, van der Velde B J, Roberts C, Woodbridge K and Hutchings K M 1991 *Semicond. Sci. Technol.* **6** 616
[33] Sasa S, Muto S and Hiyamizu S 1986 *Japan. J. Appl. Phys.* **25** L674
[34] Rauch W, Gornik E, Weimann G and Schlapp W 1991 *Semicond. Sci. Technol.* **6** 1054
[35] Mosko M, Pelouard J L and Pardo F 1994 *Semicond. Sci. Technol.* **9** 806
[36] Kane B E, Eisenstein J P, Wegscheider W, Pfeiffer L N and West K W 1994 *Appl. Phys. Lett.* **65** 3266
[37] Yoshioka D and McDonald A H 1990 *J. Phys. Soc. Japan* **59** 4211
[38] Lozovik Yu E and Yudson V I 1976 *Solid State Commun.* **19** 391
[39] Paquet D, Rice T M and Ueda K 1985 *Phys. Rev.* B **32** 5208
[40] Liu L Y, Mendez E E and Mayer H 1992 *Appl. Phys. Lett.* **60** 2971
[41] Fukuzawa T, Gustafson T K and Yamada E 1990 *IEEE J. Quantum Electron.* **26** 811
[42] Oppenheimer J R 1928 *Phys. Rev.* **13** 66
[43] Bardeen J 1961 *Phys. Rev. Lett.* **6** 57
[44] Harrison W A 1961 *Phys. Rev.* **123** 85
[45] Riechert H, Bernklau B, Reithmeier J P and Schnell R D 1991 *Resonant Tunneling in Semiconductors—Physics and Applications* (New York: Plenum) p 21
[46] Wie C R and Choy Y W 1991 *Appl. Phys. Lett.* **58** 1077
[47] Smoliner J, Gornik E and Weimann G 1988 *Appl. Phys. Lett.* **52** 2136
[48] Demmerle W, Smoliner J, Berthold G, Gornik E, Böhm G and Weimann G 1991 *Phys. Rev.* B **44** 3090
[49] Christanell R and Smoliner J 1988 *Rev. Sci. Instrum.* **59** 1290
[50] Reinacher N, Demmerle W, Smoliner J, Gornik E, Weimann G and Böhm G 1993 *J. Appl. Phys.* **74** 3593
[51] Garbow B S, Boyle J M, Dongara J J and Moler C B 1977 *Matrix Eigensystem Routines (Lecture Notes in Computer Science 51)* (New York: Springer)
[52] Stern F and Das Sarma S 1984 *Phys. Rev.* B **30** 840
[53] Hedin L and Lundquist B I 1971 *J. Phys. C: Solid State Phys.* **4** 2064
[54] Smoliner J, Berthold G, Hirler F and Reinacher N 1991 *Semicond. Sci. Technol.* **6** 642
[55] Eisenstein J P, Pfeiffer L N and West K W 1992 *Phys. Rev. Lett.* **69** 3804
[56] Eisenstein J P, Pfeiffer L N and West K W 1994 *Surf. Sci.* **305** 393
[57] Brown K M, Turner N, Nicholls J T, Linfield E H, Pepper M, Ritchie D A and Jones G C A 1994 *Phys. Rev.* B **50** 15 465
[58] Palaanen M A *et al* 1992 *Phys. Rev.* B **45** 11 342 and references therein
[59] Johanson P and Kinnaret J M 1994 *Phys. Rev.* B **50** 4671
[60] Ashoori R C, Lebens J A, Bigelow N P and Silsbee R H 1993 *Phys. Rev.* B **48** 4616
[61] Eisenstein J P, Pfeiffer L N and West K W 1995 *Phys. Rev. Lett.* **74** 1419
[62] Boebinger G S, Levi A F J, Passner A, Pfeiffer L N and West K W 1993 *Phys. Rev. Lett.* **47** 16 608
[63] Hickmott T W 1987 *Solid State Commun.* **63** 371
[64] Mendez E E, Esaki L and Wang W I 1986 *Phys. Rev.* B **33** 2893
[65] Goncalves da Silva C E T and Mendez E E 1988 *Phys. Rev.* B **38** 3994
[66] Kane B E, Tsui D C and Weimann G 1988 *Phys. Rev. Lett.* **61** 1123
[67] Smoliner J, Gornik E and Weimann G 1989 *Phys. Rev.* B **39** 12 937
[68] Suski T, Gschlössl G, Demmerle W, Smoliner J, Gornik E, Böhm G and Weimann G 1991 *Appl. Phys. Lett.* **59** 2436
[69] Mendez E E, Esaki L and Wang W I 1986 *Phys. Rev.* B **33** 2893
[70] Lebens J A, Silsbee H H and Wright S L 1988 *Phys. Rev.* B **37** 10 308
[71] Ben Amor S, Martin K P, Rascol J J L, Higgins R J, Torabi A, Harris H M and Summers C J 1988 *Appl. Phys. Lett.* **53** 2540
[72] Gueret P, Baratoff A and Marclay E 1987 *Europhys. Lett.* **3** 367
[73] Leadbetter M L, Eaves L, Simmonds P E, Toombs G A, Sheard F W, Claxton P A, Hill G and Pate M A 1988 *Solid State Electron.* **31** 707
[74] Davies R A, Newson D J, Powell T G, Kelly M J and Myron H W 1987 *Semicond. Sci. Technol.* **2** 61
[75] Hayden R K, Maude D K, Eaves L, Valdares E C, Henini M, Sheard F W, Hughes O H, Portal J C and Cury L 1991 *Phys. Rev. Lett.* **66** 1749
[76] Kesan V P, Gennser U, Syphers D A, Smith T P and Iyer S S 1993 *J. Vac. Sci. Technol.* B **11** 1140
[77] Schuberth G, Abstreiter G, Gornik E, Schäffler F and Luy

J F 1991 *Phys. Rev.* B **43** 2280
[78] Kurobe A, Castleton I M, Linfield E H, Grimshaw M P, Brown K M, Ritchie D A, Pepper P and Jones G A C 1994 *Phys. Rev.* B **50** 4889
[79] Rainer G, Smoliner J, Gornik E, Böhm G and Weimann G 1995 *Phys. Rev.* B **51** 17 642
[80] Luryi S and Capasso F 1985 *Appl. Phys. Lett.* **47** 1347
[81] Zaslavsky A, Tsui D C, Santos M and Shayegan M 1991 *Appl. Phys. Lett.* **58** 1440
[82] Dignam M M, Ashoori R C, Stoermer H L, Pfeiffer L N, Baldwin K L and West K W 1994 *Phys. Rev.* B **49** 3369
[83] Tarucha S, Hirayama Y, Saku T and Kimura T 1990 *Phys. Rev.* B **41** 5459
[84] Tarucha S, Hirayama Y and Tokura Y 1991 *Appl. Phys. Lett.* **58** 1623
[85] Bryant G W 1989 *Phys. Rev.* B **39** 3145
[86] Bryant G W 1991 *Phys. Rev.* B **44** 3782
[87] Eugster C C and del Alamo J A 1991 *Phys. Rev. Lett.* **67** 3586
[88] Eugster C C, del Alamo J A, Melloch M R and Rooks M J 1993 *Phys. Rev.* B **48** 15 057
[89] Demmerle W, Smoliner J, Gornik E, Böhm G and Weimann G 1993 *Phys. Rev.* B **47** 13 547
[90] Smoliner J, Demmerle W, Gornik E, Böhm G and Weimann G 1994 *Semicond. Sci. Technol.* **9** 1925
[91] Geim A K, Main P C, La Scala N Jr, Eaves L, Foster T J, Beton P H, Sakaki J W, Sheard F W, Henini M, Hill G and Pate M A 1994 *Phys. Rev. Lett.* **72** 2061
[92] Matveev K A and Larkin A I 1992 *Phys. Rev.* B **46** 15 337
[93] Hickmott T W 1992 *Phys. Rev.* **46** 15 169
[94] Grabert H and Devoret M (ed) 1991 *Single Charge Tunneling* (New York: Plenum)
[95] Tedwordt M, Martin-Monero L, Nicholls J T, Pepper M, Kelly M J, Law V J, Ritchie D A, Frost J E F and Jones G A C 1992 *Phys. Rev.* B **45** 14 407
[96] Reed M A, Randall J N, Aggarwal R J, Matyi R J, Moore T M and Wetsel A E 1988 *Phys. Rev. Lett.* **60** 535
[97] Boero M and Inkson J C 1994 *Phys. Rev.* B **50** 2479
[98] Bu Su, Goldman V J and Cunningham J E 1992 *Science* **255** 313
[99] Guéret P, Blanc N, Germann R and Rothuizen H 1992 *Phys. Rev. Lett.* **68** 1896
[100] Dellow M W, Beton P H, Langerak C J G M, Foster T J, Main P C, Eaves L, Henini M, Beaumont S P and Wilkinson C W D 1992 *Phys. Rev. Lett.* **68** 1754
[101] Tarucha S, Tokuta J and Hirayama Y 1991 *Rev.* B **43** 9373
[102] Tewordt M, Asahi H, Law V J, Syme R T, Kelly M J, Ritchie D A, Churchill A, Frost J E F, Huges R H and Josnes G C A 1987 *Appl. Phys. Lett.* **50** 413
[103] Fong C Y, Nelson J S, Hemstreet L A, Gallup R F, Chang L L and Esaki L 1992 *Phys. Rev.* B **46** 9538
[104] Zhen Li Ji 1994 *Phys. Rev.* B **50** 4658
[105] Tedword M *et al* 1994 *Phys. Rev.* B **49** 8071
[106] Luban M and Luscombe J H 1990 *Appl. Phys. Lett.* **57** 61
[107] Bryant G W 1991 *Phys. Rev.* B **44** 12 838
[108] Tekman E and Ciraci S 1989 *Phys. Rev.* B **40** 8559
[109] Kamata N, Yamada K and Miura N 1993 *J. Phys. Soc. Japan* **62** 2120
[110] Sa'ar S, Feng J, Grave I and Yariv A 1992 *J. Appl. Phys.* **72** 3598
[111] Gobato Y G, Berroir J M and Gouldner Y 1993 *Solid State Commun.* **87** 513